CHEMISTRY OF MATERIALS

Article

pubs.acs.org/cm

$ZrSe_3$-Type Variant of TiS_3: Structure and Thermoelectric Properties

Emmanuel Guilmeau, David Berthebaud, Patrick R. N. Misse, Sylvie Hébert, Oleg I. Lebedev, Daniel Chateigner, Christine Martin, and Antoine Maignan*

Laboratoire CRISMAT, UMR 6508 CNRS/ENSICAEN/UCBN, 6 bd du Maréchal Juin, F-14050 Caen Cedex 4, France

ABSTRACT: A dense TiS_3 sample has been processed by Spark Plasma Sintering. The structural analysis, obtained by coupling powder X-ray diffraction and transmission electron microscopy (TEM), shows that the A-variant of the $ZrSe_3$-type structure is stabilized for the first time. Defects along the main atomic layer stacking directions are evidenced by high-resolution TEM, which explain the peculiar X-ray powder diffraction patterns, with strongly anisotropic microstrains. The presence of these structural defects might explain the existence of a metal-to-insulator transition with a charge localization below $T_{MI} \approx 325$ K. Large absolute values of the Seebeck coefficient, in the range $-700 \leq S \leq -600$ $\mu V \cdot K^{-1}$, are observed for $100 \leq T \leq 600$ K, together with a low thermal conductivity, $\kappa = 2$ $W \cdot K^{-1} \cdot m^{-1}$ at 600 K. The T^{-1} dependence of the lattice part of κ indicates its phononic character. As the charge carrier concentration measured by Hall effect is too low, $n = 1.24 \times 10^{18}$ cm^{-3}, extra doping would be necessary to decrease its too high electrical resistivity ($\rho_{300K} \sim 1.4$ $\Omega \cdot cm$) for thermoelectric applications.

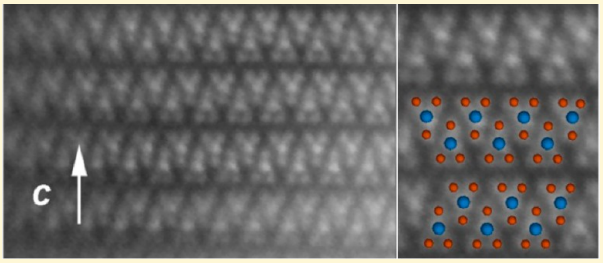

INTRODUCTION

When looking for alternative thermoelectric materials, the toxicity, the weight, and the cost issues are important concerns. This explains why Mg_2Si and its derivatives are under the scope as Mg and Si are abundant, light, and nontoxic elements.[1] As so, the TiS_2 sulfides, with intercalated chemical species between successive TiS_2 slabs, are also revisited.[2,3] Recently, zT values as high as 0.45 were reported for Cu_xTiS_2[4] (zT is the adimensional figure of merit, where T is the absolute temperature and $z = S^2/\rho\kappa$ with S, ρ, and κ being the Seebeck coefficient, electrical resistivity, and thermal conductivity, respectively). Interestingly, this layered sulfide can be viewed as a realization of the PGEC concept (PGEC = phonon glass and electron crystal)[5] as the TiS_2 slab is conducting and the intercalated species are found to reduce the phonon part of the thermal conductivity. As the decrease of the structural dimensionality is also a way to increase the Seebeck coefficient by the so-called quantum confinement phenomenon, our attention was attracted by the TiS_3 compound. A large Seebeck value of about $S \sim -700$ $\mu V \cdot K^{-1}$ at 300 K was reported for a TiS_3 crystal, with a high electrical resistivity, $\rho_{300K} = 2$ $\Omega \cdot cm$,[6] but its thermal conductivity was not studied. In addition, very few studies have been reported on the crystal structure.[7,8]

In their pioneering work, Furuseth and others showed the structural complexity of the MX_3 trichalcogenides with principally M = Ti, Zr, or Hf and X = S, Se, or Te.[7,8] Indeed, depending on the [M,X] couple, two very close structures are stabilized, noted A ($ZrSe_3$-type) and B (TiS_3-type) (Figure 1a,b, respectively), belonging both to the $P2_1/m$ space group with similar lattice parameters ($a \approx 5$ Å, $b \approx 3.5$ Å, and $c \approx 9$ Å with $\beta \approx 97.5°$). As also shown by this figure, the layer stacking along $\vec{c}$ is characterized by the presence of X bilayers bonded by van der Waals forces[9] that gives, at least, a 2D character to the structure. The M cations form skirt triangular lattices with different distributions of the M−M distances between A- and B-variants (Figure 2a,b), leading to consideration of M chains or M triangular ladders, respectively, both running along $\vec{b}$. The scattering of the M−X distances is another parameter that differentiates both structures: it is larger for the B-type with a more distorted X environment around M (Figure 1a,b).

Concerning the phonon part of the thermal conductivity (κ_{ph}), as the disorder in the chemical bonding is expected to favor a low κ_{ph}, TiS_3 is an interesting candidate to be measured. Furthermore, up to now no link between structural parameters and properties was established on TiS_3 polycrystals and the spark plasma sintering (SPS) technique offers new synthesis conditions, particularly attractive in that case because its fastness allows both reaching nearly 100% compacity and limiting the grain growth. In the following, we report on TiS_3 ceramic synthesis using SPS, its structural analysis using X-ray powder diffraction and transmission electron microscopy, and its thermoelectric properties.

EXPERIMENTAL SECTION

A precursor was first prepared by solid-state reaction between Ti and S (99.5%, Alfa Aesar) in an evacuated tube sealed within a primary vacuum of 10^{-3} bar at 600 °C, with similar heating and cooling rates of 100 °C/h. Compared to TiS_3, a sulfur excess corresponding to a 1:4 Ti:S ratio was used to avoid the formation of TiS_2. The obtained powder, containing TiS_3 and sulfur, was subsequently densified in a primary vacuum using a SPS machine (FCT HPD 25). About 6 g of this powder was poured into a graphite mold (inner diameter 15 mm) and sintered at 600 °C for 10 min under 50 MPa (heating rate 100 °C/h). The graphite surface layer of the as-synthesized pellet was then removed, and pieces with different shapes and sizes were cut for the following characterizations,

Received: June 6, 2014
Revised: August 26, 2014
Published: September 3, 2014

   dx.doi.org/10.1021/cm502069n | Chem. Mater. 2014, 26, 5585−5591

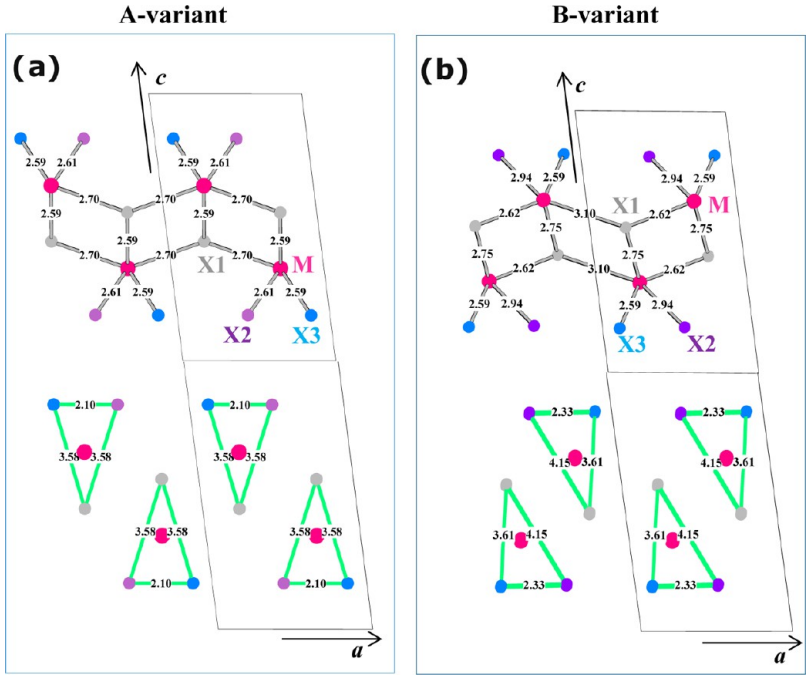

Figure 1. Schematic views of the A- and B-variants, using crystallographic parameters reported for HfS_3 (a) and $HfSe_3$ (b), respectively.[8] [010] projection in this figure: four cells are shown, with the M−X distances in the upper part and the X−X distances delimiting triangle around M in the lower cells (to highlight the difference between both variants and that will be exploited for the TEM study).

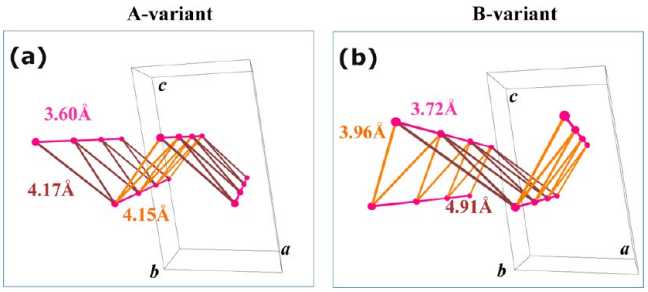

Figure 2. Schematic views of the A- and B-variants, using crystallographic parameters reported for HfS_3 (a) and $HfSe_3$ (b), respectively.[8] M lattice is drawn here to give arguments in the discussion on the dimensionality of this type of compounds.

in such a way that all electrical and thermal measurements have been done in the plane of the pellet, that is, perpendicular to the applied pressure axis P_{SPS} used during the sintering step. The measured densities were greater than 95% of the theoretical value.

X-ray powder diffraction (XRPD) was performed at room temperature using a $\theta-2\theta$ measurement on a D8 Bruker diffractometer with Cu Kα_1 radiation (λ_1 = 1.5406 Å), in reflection geometry with a parallel beam. Fullprof[10] and Maud[11] software were used to analyze the structural data on powders of the SPS-elaborated bulk, respectively. We used the Popa model[12] to represent the mean crystallite sizes and shapes, using anisotropic microstrains, and a spherical harmonic model to take into account the fiber textures induced during sample mounting.[13] The instrument resolution was calibrated with a LaB_6 powder standard from NIST.

The electrical resistivity (ρ) and Seebeck coefficient (S) measurements were performed using a four-probe method and steady-state techniques, respectively, on 10 × 2 × 2 mm samples. Temperature dependencies of ρ and S were simultaneously carried out from 300 to 700 K by means of an ULVAC-ZEM3 system (under partial He pressure). Thermal diffusivity of a square sample (6 × 6 × 1 mm) was measured from 300 to 700 K in an inert atmosphere using a Netzsch LFA457 apparatus. Thermal conductivity (κ) was obtained from the product of the sample density, thermal diffusivity, and heat capacity, the latter being calculated with the Dulong-Petit approximation. The low-temperature ρ and S measurements were performed in a Quantum Design PPMS (Physical Properties Measurements System) with similar type of bar as for the high-T S and ρ measurements. A homemade sample holder was used to measure ρ by the four-probe technique (using indium contacts) and S (steady-state technique). Hall effect at 300 K was also measured in the PPMS with a magnetic field, up to 9 T, applied perpendicular to the plane of the sample (along P_{SPS}) with 2 × 2 × 0.2 mm dimensions.

Transmission electron microscopy (TEM), electron diffraction (ED), and high-resolution TEM (HRTEM) studies were carried out using a FEI Tecnai G2 30 UT microscope operated at 300 kV and having 0.17 nm point resolution. The chemical composition of the main TiS_3 phase was verified by EDX analysis using an attached EDAX system. High-angle annular dark-field STEM (HAADF-STEM) experiments were carried out on an aberration-corrected JEM ARM200F microscope operated at 200 kV equipped with a CENTURIO EDX detector. The TEM specimens from the bulk precursor and dense SPS samples were prepared in the same way by grinding in an agate mortar, dissolving in methanol, and spread on the holey carbon grid.

RESULTS

Structural Features. At first, the room-temperature XRPD pattern reveals that the TiS_3 phase forms with only a few additional small peaks attributed to traces of S_x and TiS_2 (Figure 3) that validates the process used for preparing the sample. A Le Bail fit confirms the $P2_1/m$ space group with the following cell parameters, a = 4.9680(1) Å, b = 3.401(1) Å, c = 8.810(2) Å, and β = 97.821(2)°. Though there exists a strong broadening of numerous Bragg peaks, as highlighted in the left inset of Figure 3, all the 00l are narrower than others. This indicates an anisotropic disorder with either larger coherent domains or lower levels of microstrains along the c-axis than along other directions of the crystals. TiS_3 is supposed to be of the B-type variant,[8] the XRPD pattern of which is simulated in the right inset of Figure 3. Even by allowing line broadening to take into account the shape variations of hkl peaks, the simulation of the observed pattern is

dx.doi.org/10.1021/cm502069n | Chem. Mater. 2014, 26, 5585−5591

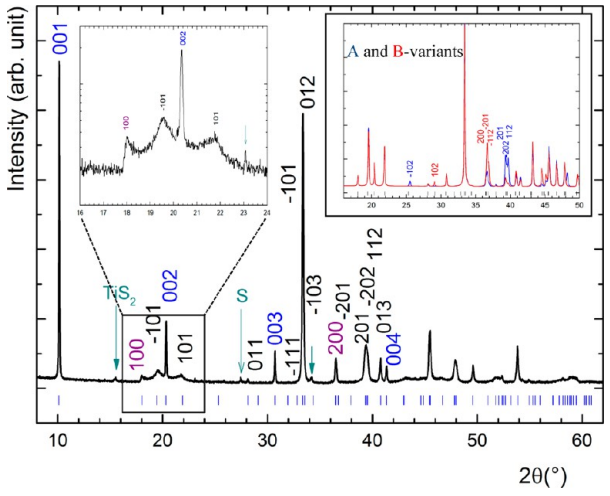

Figure 3. X-ray powder diffraction pattern of TiS_3, the indexation of the main first Bragg peak is given ($P2_1/m$ and a = 4.968 Å, b = 3.401 Å, c = 8.810 Å, and β = 97.821°), and the impurities are identified by arrows. An enlargement between 16° and 24° in 2θ is given in the inset (left) with a logarithmic scale for the y-axis (intensity) to highlight the broadening of some peaks. In the right inset are shown the calculated XRPD patterns of A- and B-variants (without any broadening).

very difficult to carry out: as an example, the intensity ratio of the (200, −201, and −112) and (201, −202, and 112) sets of peak is opposite to what is expected. In contrast, building an A-variant model leads to a more appropriate calculated diffractogram (as shown in the right inset of Figure 3). Before going ahead by using this hypothesis as a starting point for calculations, TEM investigations were undertaken.

The low-magnification images (Figure 4) show the tape shape of the microcrystals: the longest dimension is along the b-axis (≈ 30 μm), the width and thickness of the tapes are ≈5 and 1.5 μm, respectively, and the c-axis is perpendicular to the figure surface. ED patterns taken along the main zone axes (Figure 5) confirm the good crystallinity of the sample, the $P2_1/m$ space group and cell parameters given above. The corresponding EDX analysis leads to the expected TiS_3 composition.

To confirm by XRPD calculation the proposed A-variant structure, HAAD-STEM imaging along the [010] zone axis was carried out. As shown in Figure 1a,b, in principle, the [010] direction allows distinguishing between the variants. HAADF-STEM (or so-called Z-contrast imaging) is mass−thickness sensitive, having image contrast in atomic resolution images that scales with the atomic number $Z^{\sim 1.7}$. As it is an incoherent imaging technique, diffraction contrast will not hinder the interpretation of the images like in the case of HRTEM imaging where the too complicated contrast does not allow revealing the differences between the variants. Figure 6 shows high-resolution HAADF-STEM images of TiS_3 crystallite along [010] zone axis which clearly shows different positions of Ti (brighter dots, Z = 22) and S (bright dots, Z = 16) atomic columns. The structural model of the A-variant (shown in the left bottom panel) is overlaid on the enlargement, matching perfectly with the acquired images. This unambiguously confirms the proposed A-variant structure, supporting the preliminary XRPD analysis. Obviously, the B-variant model (right bottom panel) would not match with the experimental image.

Also, it is important to notice a significant amount of stacking faults, with (00l) planes of the A-variant structure shifting along the [100] direction at the level of the sulfur double layer. These shifts can be explained by the weak S−S bonding through the van der Waals gap. This creates slices of A-type TiS_3 structure having

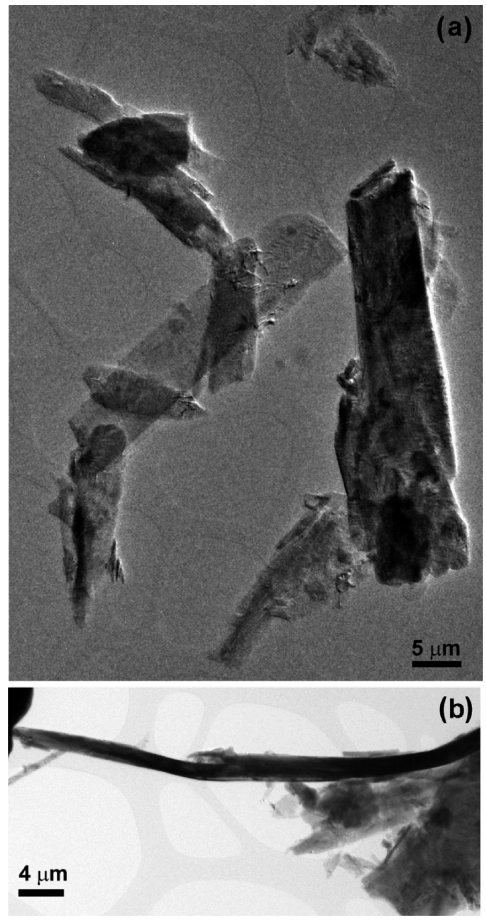

Figure 4. (a) Low-magnification bright-field TEM images of powder TiS_3. (b) Note the typical tape-type morphology of the crystallite with a thickness of a few micrometers along the c-axis.

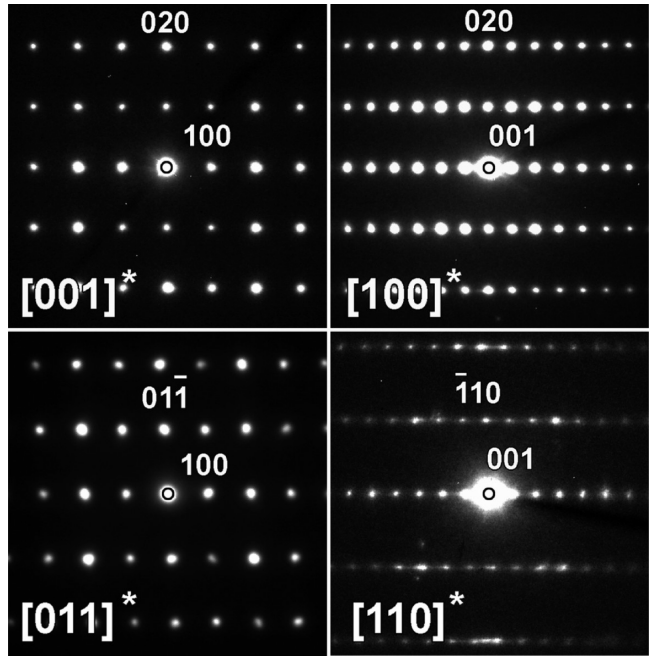

Figure 5. ED patterns of TiS_3 along the main zone axis and indexation within the $P2_1/m$ space group.

thickness of (5 ± 2) × c (Figure 7, white arrows). Such shifts correspond to planar defects, randomly spaced along c*, without

dx.doi.org/10.1021/cm502069n | Chem. Mater. 2014, 26, 5585−5591

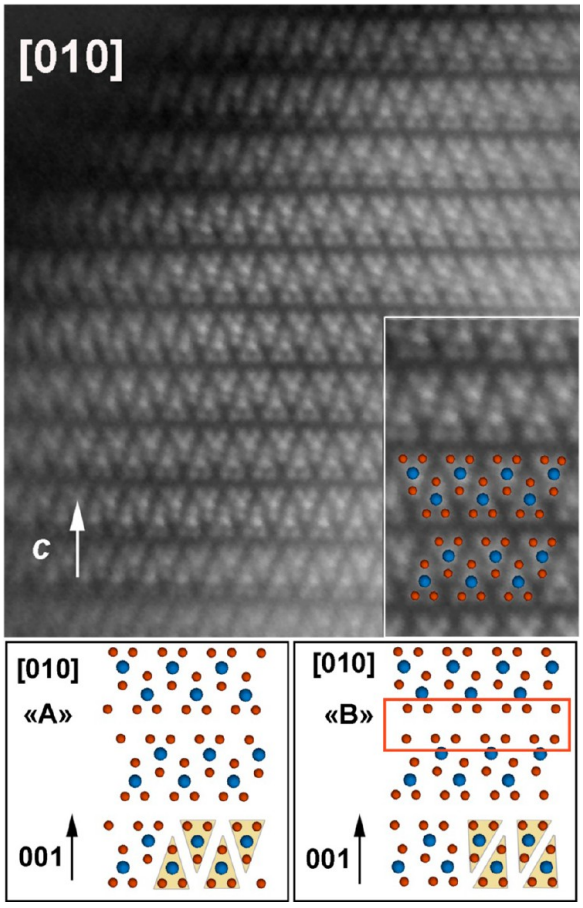

Figure 6. High-resolution [010] HAADF-STEM image of TiS_3 and two possible structure models: A-variant (left bottom panel) and B (right bottom panel) viewed along [010] zone axis. Enlargement together with overlay A-variant structure is given as insert and shows a perfect matching of the experimental HAADF-STEM image with the A-variant structural model. In the right bottom panel, the rectangle surrounding the sulfur double layer illustrates the difference in the S atomic positions between the variants.

inducing large wave incoherence along this direction, that is, not introducing severe 00l line broadening. In Figure 7, when compared to the A-variant structural model (right bottom figure), the shift of the S layers at the level of the defect (surrounded by a rectangle), corresponds to S positions closer to those of B-variant structure (right bottom panel in Figure 6).

The [100] HRTEM images reveal also another kind of defective region (Figure 8a). Despite an overall perfect crystal structure, defects, like misfit dislocations or disordered regions (marked by ⊥ and white arrows, respectively), are observed. An example of a highly defective region is given in Figure 8b. In this area, we also observe progressively inclined {00l} planes looking like bending. This internal waving of the structure does not change the spacing along the *c*-axis but should shift the atoms from ideal positions of A-variant structure in the bending area. This should create microstrains in this material. All these defects are again not believed to introduce significant {00l} line broadening, keeping X-ray wave coherency along *c**. However, this is not the case of other {*hkl*} lines, for which coherence length is perturbed, and consequently broadened due to all defect types in a complex scheme.

Then the Maud software was used in an attempt to approach the line broadening as close as possible. This approach allows a quite reasonable fit of the pattern (Figure 9a), together with

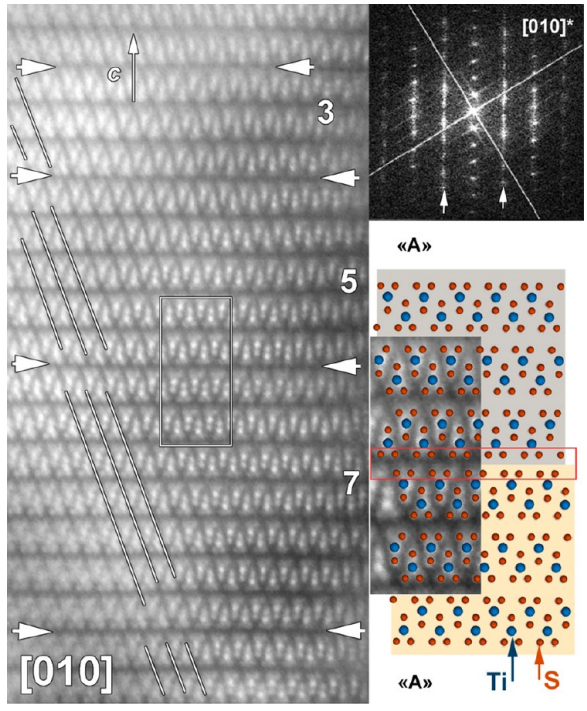

Figure 7. High-resolution [010] HAADF-STEM image of a region containing planar defects. Clear shifts along $\vec{c}$ (stacking direction) of successive planes (marked by white lines) are evidenced between A-variant structural blocks of different widths. Numbers are indicated width in unit cells. The oblique white lines are guides to the eyes to evidence the shifts between the blocks along $\vec{a}$.

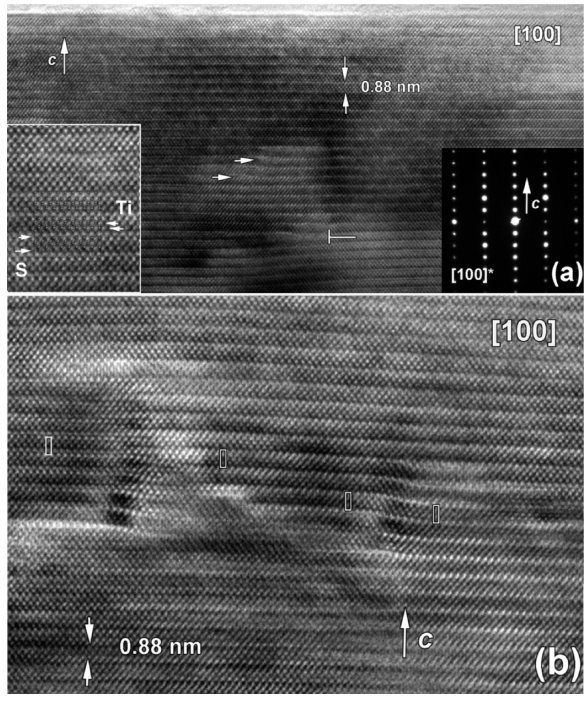

Figure 8. (a) Bright-field [100] HRTEM image of SPS TiS_3 sample viewed along the *c*-axis and corresponding ED pattern. Misfit dislocation is marked. Enlargement HRTEM image as inset. (b) [100] HRTEM image of defect region.

evidence for a weak texture in the sample, with {00l} and {l00} planes preferentially aligned with the sample plane (Figure 9b), and also a maximum orientation density of 1.6 M.R.D.

dx.doi.org/10.1021/cm502069n | *Chem. Mater.* 2014, 26, 5585−5591

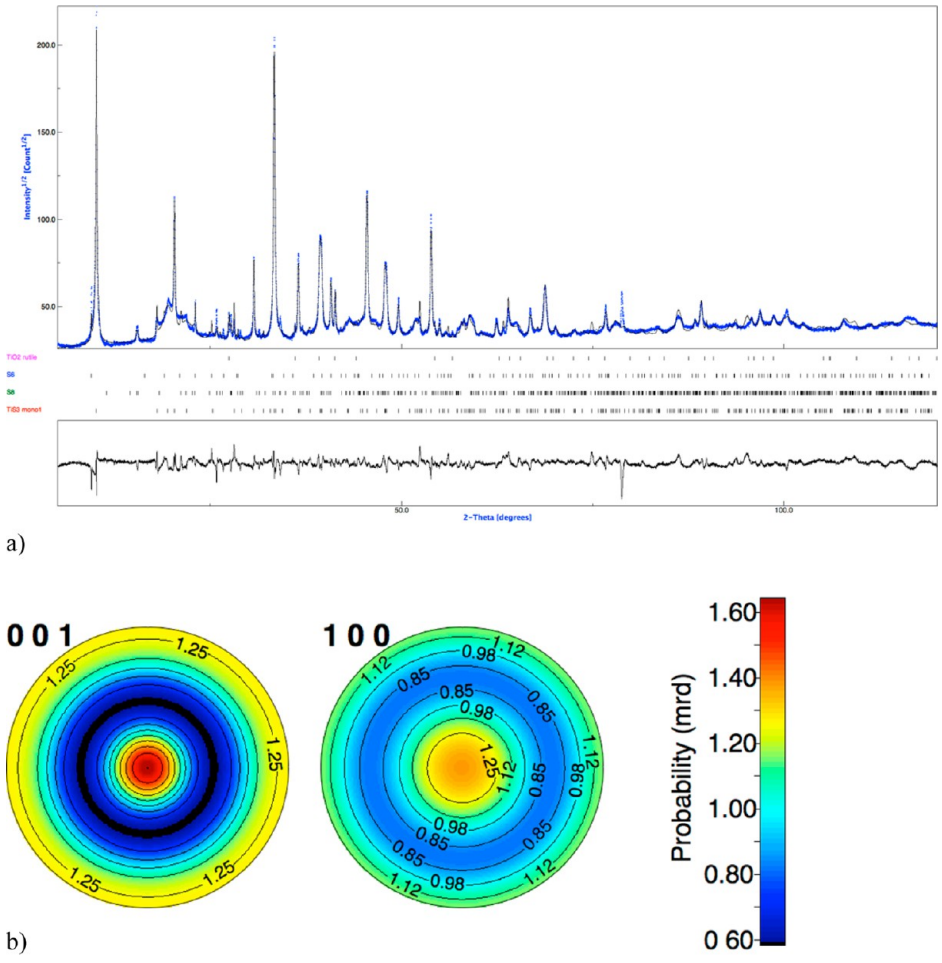

Figure 9. (a) XRD diagram measured on powder of the SPS bulk sample, and corresponding Rietveld fit, operated with anisotropic crystallite sizes and microstrains, and weak preferred orientation. (b) Corresponding {001} and {100} pole figures obtained from spherical harmonics.

(multiple of a random distribution) only. Such texture levels are usual when mounting samples made of platelet-like crystals in reflection mode. The Popa analysis results in mean parallelepiped-like crystallite shapes with 1900 × 880 × 900 Å^3 along *a*-, *b*-, and *c*-axes, respectively. These mean dimensions are much smaller than the apparent crystals visible in Figure 4 because they correspond to the mean coherent size domains, diffraction coherency being destructed by intrinsic defects. However, such crystallite sizes cannot account alone for the observed peak broadenings and produce diffraction peaks as narrow as the 00*l*'s, and no fit improvement. A refinement allowing anisotropic microstrains determination considerably improves the fit (Figure 9a). Interestingly, the determined microstrains appeared much lower (1 order of magnitude or more) along [001] (3.5×10^{-4} rms) than along other main and inclined directions (1.4×10^{-3} along [100]; 5.5×10^{-3} along [−101], for instance). An attempt to introduce turbostratic disordering in the Rietveld refinement using the Ufer model,[14] which could appear reasonable from the observation of the strong right-hand side asymmetry of the 100 line, appeared detrimental to the fit.

On a structural point of view (Figure 10), taking into account the broadened intensities moderately distorts the structural model. Comparing the "defect-free" structural analysis at the local scale (HRTEM study of Figure 6) and at macroscopic scale with incorporation of all defect types in the pattern (Figure 10) then helps picturing the role of defects in experimental signatures. Though the defective areas at crystallite boundaries are responsible for the apparent distortion of the A-type structure (Figure 10a), the Ti network with the shortest Ti−Ti distances along *b* (Figure 10b) keeps the A-type feature with Ti−Ti chains rather than ladders.

The phonon thermal conductivity is expected to be low as a result of phonons propagation hindered by the intrinsic disorder in the Ti−S bonds and at the level of the planar defects. For the A-variant (ref 8), there exist three S positions, S_1, S_2, and S_3. Each Ti^{4+} cation is bonded to four S_1 atoms (Figure 1), with three different Ti−S_1 interatomic distances, and two S_2 and two S_3 atoms. Moreover, the S_2−S_3 short distances (~2 Å) indicate that $(S_2S_3)^{2-}$ dianions are formed. Consequently, the Ti−S bonds can be viewed as a mixture of Ti−S and Ti−(S_2S_3) bonds, that is, ligands of different mass which, in principle, is good in order to limit κ_{ph}.

Physical Properties. The electrical resistivity (Figure 11a and Table 1) exhibits a metal ($T > T_{MI}$) to insulator ($T < T_{MI}$) transition with a minimum value of 1.2 Ω·cm at T_{MI} = 325 K. It must be pointed out that the localization observed below T_{MI} leads to too large ρ values ($\rho > 10^6$ Ω·cm) below $T \sim 25$ K for our experimental setup. The room-temperature value, ρ_{300K} = 1.4 Ω·cm, is very similar to that reported along the chain direction for crystal whiskers, with ρ_{300K} = 2 Ω·cm,[15] or crystals with ρ = 3 Ω·cm.[6]

Nonetheless, our T_{MI} value is larger by about 100 K as compared to those in previous studies,[6,15] which might reflect a larger defect concentration or possible effects coming from the variant nature of our ceramic sample. As the TEM results reveal the

dx.doi.org/10.1021/cm502069n | *Chem. Mater.* 2014, 26, 5585−5591

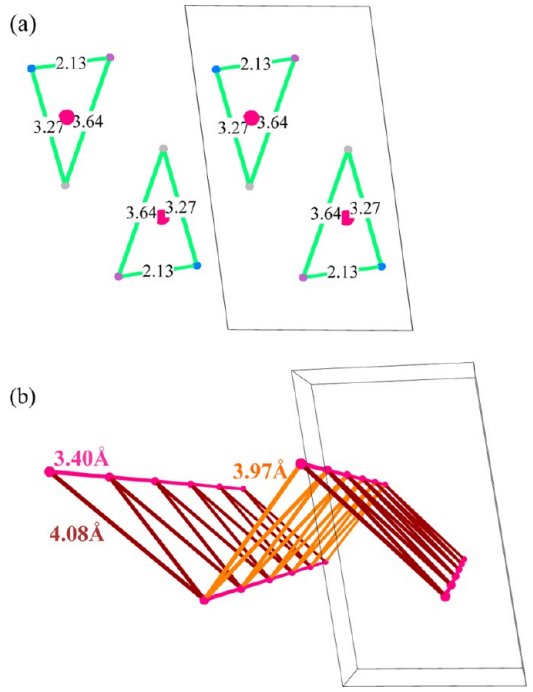

Figure 10. (a) [010] projection (as in Figure 1) of the structure refined from the diagram in Figure 9, with incorporation of defect and texture models in the fit, and S−S distances. (b) Corresponding Ti lattice with the Ti−Ti distance. The distance along *b* is the shortest, showing that the Ti network is made of chains rather than ladders.

presence of numerous defects along the direction of the Ti chains (*b*-axis, Figure 8b), this might affect the electronic conduction properties. Indeed, the structural disorder was involved to explain the localization effect in TiS_3;[6] our results support this scenario.

When one compares ρ for TiS_2 and TiS_3 (Table 1), the larger value of the latter suggests a lower charge carrier concentration. For that purpose, we estimated the latter using Hall effect measurements. The value at 300 K leads to $n = 1.24 \times 10^{18}$ cm^{-3}, a value slightly smaller than $n = 2 \times 10^{18}$ cm^{-3} deduced from Hall effect measurements on crystals.[9]

Concerning the thermopower, the $S(T)$ curve (Figure 11a) reveals rather limited S change with T for a broad range of T with values in the range −700 to −600 μV·K^{-1} for $100 \leq T \leq 600$ K, indicating n-type behavior. Nonetheless, slight changes can be detected near 375 K, which can be associated with the melting point of the remaining sulfur (388 K), and for $T > 600$ K, the $S(T)$ curve starts to diverge which could indicate that TiS_3 starts to decompose in TiS_2. It must be emphasized that the existence of a ρ minimum at $T_{MI} = 325$ K is not related to the sulfur melting temperature. This confirms the intrinsic nature of this transition. As for thermoelectric applications, the adimensional figure of merit is defined as $zT = (S^2/\rho\kappa) \times T$, the thermal conductivity κ was also measured but only above 300 K (Figure 11b). κ is found to decrease by almost a factor of 2 as T increases from 300 to 600 K, reaching a low value of 2 W·K^{-1}·m^{-1} at 600 K. According to the Wiedemann−Franz law, the too high electrical resistivity values make that the total thermal conductivity is mainly dominated by the lattice part. Over all of the investigated T range, κ follows a T^{-1} dependence (Figure 11b, right *y*-axis), which is characteristic of phonons with Umklapp processes. The corresponding power factor (PF = $S^2/\rho\kappa$) and zT values are given in Figure 11c.

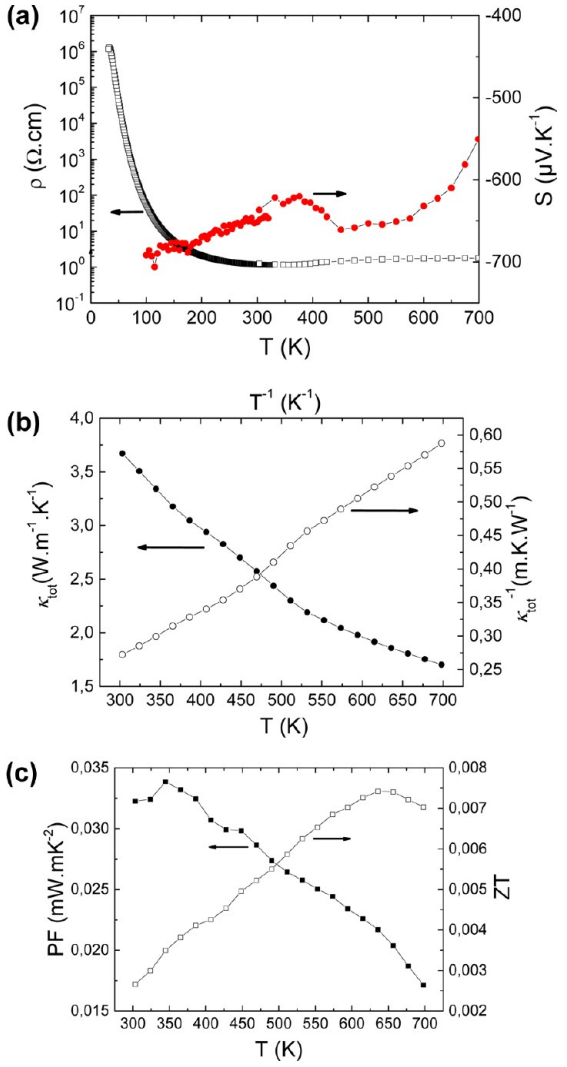

Figure 11. (a) T-dependence of the electrical resistivity ρ (left *y*-axis) and Seebeck coefficient S (right *y*-axis). (b) Total thermal conductivity κ as a function of T (lower *x*-axis and left *y*-axis) and T^{-1} (upper *x*-axis and right *y*-axis). (c) T dependence of both power factor (PF, left *y*-axis) and figure of merit (zT, right *y*-axis).

DISCUSSIONS

The present study shows that a ceramic of TiS_3 A-variant can be prepared by the SPS technique. Starting from a precursor containing extra sulfur, a rather stoichiometric TiS_3 compound is obtained with a large absolute S value at 300 K, $|S| = 650$ μV·K^{-1}, similar to that reported for a TiS_3 crystal,[6] corresponding to a small charge carrier concentration. In a previous report,[16] the electronic band structure, probed on crystals by XPS, indicated the existence of a gap with empty d_z2 orbitals contrasting with the partially filled d_z2 orbitals in metallic TaS_3. This reflects the empty character of the $3d^0$ orbitals for Ti^{4+} according to the $Ti^{4+}S^{2-}(S_2)^{2-}$ formal formula. However, the characteristic temperature of the resistivity minimum at the metal−insulator transition for the TiS_3 ceramic is shifted up by about 100 K as compared to that of crystals.[6,15] This could result from the large content of structural defects, evidenced by the present electron microscopy study, which is probably favored by the short reaction time of the SPS process. Moreover, the lack of change in the Seebeck coefficient at T_{MI} is in marked contrast with the behavior evidenced for TaS_3, which exhibits a spin Peierls

dx.doi.org/10.1021/cm502069n | Chem. Mater. 2014, 26, 5585−5591

Table 1. TiS_3: Parameters Extracted from the $\rho(T)$, $S(T)$, and $\kappa(T)$ Curves[a]

				TiS_3				
n_{300K} (Hall effect)	T_{MI} (K)	$\rho_{min}(T_{MI})$ (Ω·cm)	$S(T_{MI})$ (μV·K^{-1})	ρ_{600K} (Ω·cm)	S_{600K} (μV·K^{-1})	ρ_{300K} (Ω·cm)	S_{300K} (μV·K^{-1})	κ_{325K}, κ_{600K} (W·m^{-1}·K^{-1})
1.24×10^{18} (cm^{-3})	325	1.2	−630	2.0	−630	1.4	−650	3.7, 2.0
				TiS_2				
n_{300K} (Hall effect)	T_{MI} (K)	$\rho_{min}(T_{MI})$ (Ω·cm)	$S(T_{MI})$ (μV·K^{-1})	ρ_{600K} (Ω·cm)	S_{600K} (μV·K^{-1})	ρ_{300K} (Ω·cm)	S_{300K} (μV·K^{-1})	κ_{latt}(325 K), κ_{latt}(600 K)
0.65×10^{21} (cm^{-3})				5×10^{-3}	−245	1.5×10^{-3}	−150	3.3, 2.3

[a]Data for a SPS-prepared TiS_2 ceramic (taken from ref 4) are also given.

transition at T_p = 210 K.[17] This supports the conclusions of ref 6 that the metal-to-insulator transition is driven by structural disorder rather than a charge density wave transition.

When compared to doped TiS_2, the power factor (PF = S^2/ρ) at 300 K of TiS_3 is smaller by about 2 orders of magnitude, PF = 0.032 mW·m^{-1}·K^{-2} (Figure 11c) and PF = 1.7 mW·m^{-1}·K^{-2} for TiS_3 and TiS_2,[4] respectively. The higher value found in TiS_3 is explained by charge localization and/or small charge carrier concentration, leading to a much larger resistivity [at 300 K, ρ = 1.4 Ω·cm and ρ = 1.5 mΩ·cm for SPS-prepared TiS_3 and TiS_2 (Table 1), respectively]. As suggested in ref 6, the disorder is playing a major role. From high-resolution microscopy, the existence of several defects, and peculiarly those bending the Ti−Ti planes along the *b*-axis, supports this hypothesis.

Interestingly, despite a more complex structure with larger distribution in the Ti−S distances and numerous structural defects—such as shifts of the S planes at the level of the S bilayers or bending of the atomic layers—the lattice part of thermal conductivity of TiS_3 is similar to that of TiS_2[4]: at 600 K, $\kappa_{latt} \approx$ 2.0 W·m^{-1}·K^{-1} for both titanium sulfides. Interestingly, these κ_{latt} values are higher than those obtained by cation intercalation in TiS_2, as in $Cu_{0.1}TiS_2$, which exhibits at 600 K a κ_{latt} value of 0.9 W·m^{-1}·K^{-1}.[4] This result is important as it suggests that similar intercalation experiments as those performed in TiS_2 have to be tried for TiS_3 to increase the charge carrier concentration and hinder the phonon propagation. In the present pristine phase, despite a low thermal conductivity, the too low PF values lead to zT values (Figure 11c) that remain almost 2 orders of magnitude smaller than those of the TiS_2 dichalcogenide.

CONCLUSION

On the one hand, despite relatively low thermal conductivity values and a large absolute value of its Seebeck coefficient at high temperatures, the present TiS_3 dense ceramic exhibits power factor values too low to be of interest for thermoelectricity applications. When compared to TiS_2, this could result from too large values for the electrical resistivity related to a small charge carrier concentration. Accordingly, chemical substitutions/intercalations are now needed to create more charge carriers. However, the existence of intrinsic defects along the chains might be redhibitory to reach much higher conductivity values in this titanium trichalcogenide. On the other hand, the present structural study of SPS-prepared ceramic evidences the possibility to stabilize for the first time the A-variant for TiS_3. No significant differences in the properties could be evidenced between A- and B-variants, except the shift in the characteristic temperature of the metal-to-insulator transition but which origin is related to structural defects. Finally, considering the Ti network in the A structural type, forming chains along the *b*-direction against ladders in the B-variant along the same crystallographic direction, measurements along *b* on crystals would be necessary to compare the transport properties of the A- and B-variants.

AUTHOR INFORMATION

Corresponding Author

*E-mail: antoine.maignan@ensicaen.fr. Telephone: 33(0) 2.31.45.26.34. Fax: 33(0)2.31.95.16.00.

Notes

The authors declare no competing financial interest.

ACKNOWLEDGMENTS

The authors thank Dr. S. Gascoin for numerous XRPD collections.

REFERENCES

(1) Zaitsev, V. K.; Fedorov, M. I.; Gurieva, E. A.; Eremin, I. S.; Konstantinov, P. P.; Yu, A.; Samunir; Verdenikov, M. V. *Phys. Rev. B* **2006**, *74*, 045207.

(2) Imai, H.; Shimakawa, Y.; Kubo, Y. *Phys. Rev. B* **2001**, *64*, 241104.

(3) Wan, C.; Wang, Y.; Koumoto, K. *Materials* **2010**, *3*, 2606.

(4) Guilmeau, E.; Bréard, Y.; Maignan, A. *Appl. Phys. Lett.* **2011**, *99*, 052107.

(5) Nolas, G. S.; Morelli, D. T.; Tritt, T. M. *Annu. Rev. Mater. Sci.* **1999**, *29*, 89.

(6) Hsieh, P. L.; Jackson, C. M.; Grüner, G. *Solid State Commun.* **1986**, *46*, 505.

(7) Brattas, L.; Kjekshus, A. *Acta Chem. Scand.* **1972**, *26*, 3441.

(8) Furuseth, S.; Brattas, L.; Kjekshus, A. *Acta Chem. Scand. A* **1975**, *29*, 623.

(9) Gorochov, O.; Katty, A.; Le Nagard, N.; Levy-Clément, C.; Schleich, D. M. *Mater. Res. Bull.* **1983**, *18*, 111.

(10) Rodriguez-Carvajal, J. Fulprof. http://www.ill.eu/sites/fullprof/php/programs.html.

(11) Lutterotti, L. *Phys. Res. B* **2010**, *268*, 334−340.

(12) Popa, N. *J. Appl. Crystallogr.* **1998**, *31*, 176−180.

(13) Bunge, H.-J., Ed. *Texture Analysis in Material Science: Mathematical Methods*; Cuvillier: Göttingen, 1993.

(14) Ufer, K.; Roth, G.; Kleeberg, R.; Stanjek, H.; Dohrmann, R.; Bergmann, J. *Z. Kristallogr.* **2004**, *219*, 519−527.

(15) Gorlova, I. G.; Pokrovskii, V. Ya.; Zybtsev, S. G.; Titov, A. N.; Timofeev, V. N. *J. Exp. Theor. Phys.* **2010**, *138*, 298.

(16) Endo, K.; Ihara, H.; Watanabe, K.; Gonda, S. *J. Solid State Chem.* **1981**, *39*, 215.

(17) Dian-lin, Z.; Shu-yuan, L.; Jin, B. J.; Chu, C. W. *Phys. Rev. B* **1988**, *37*, 4502.